# Structural and double magnetic transitions in the frustrated spin-$\frac{1}{2}$ capped-kagome antiferromagnet $(RbCl)Cu_5P_2O_{10}$

S. Mohanty [1], J. Babu [2], Y. Furukawa [2], and R. Nath [1,*]

[1]*School of Physics, Indian Institute of Science Education and Research, Thiruvananthapuram 695551, India*

[2]*Ames National Laboratory and Department of Physics and Astronomy, Iowa State University, Ames, Iowa 50011, USA*

(Received 23 July 2023; accepted 14 September 2023; published 27 September 2023)

The structural and magnetic properties of the geometrically frustrated spin-$\frac{1}{2}$ capped-kagome antiferromagnet $(RbCl)Cu_5P_2O_{10}$ are investigated via temperature-dependent x-ray diffraction, magnetization, heat capacity, and $^{31}$P NMR experiments on a polycrystalline sample. It undergoes a structural transition at around $T_t \simeq 310$ K from a high-temperature trigonal ($P\bar{3}m1$) to a low-temperature monoclinic ($C2/c$) unit cell, where the low-temperature structure features the capped-kagome geometry of $Cu^{2+}$ ions. Interestingly, it shows the onset of two successive magnetic transitions at $T_{N1} \simeq 20$ K and $T_{N2} \simeq 7$ K. The shape of the $^{31}$P NMR spectra unfolds the possible nature of the transitions below $T_{N1}$ and $T_{N2}$ to be of incommensurate and commensurate antiferromagnetic type, respectively. A large value of the Curie-Weiss temperature as compared to $T_{N1}$ sets the frustration parameter $f \simeq 8$, ensuring strong magnetic frustration in the compound. From the $^{31}$P NMR spin-lattice relaxation rate, the leading antiferromagnetic exchange coupling is estimated to be $J/k_B \simeq 117$ K. These unusual double magnetic transitions make this compound beguiling for further investigations.

DOI: 10.1103/PhysRevB.108.104424

## I. INTRODUCTION

Recently, geometrically frustrated magnets have received enormous attention because of their potential to host a rich variety of magnetic and structural phases under different conditions [1,2]. One of the most engrossing ground states is the quantum spin liquid (QSL), a highly entangled and dynamically disordered state, lacking magnetic long-range order (LRO) [3]. Among different frustrated magnets, triangular lattice is the simplest example of a geometrically frustrated magnet where the spins are arranged at the vertices of a triangle, defying the antiparallel arrangements, and leading to magnetic frustration. In a triangular lattice, the triangles are edged shared to form a two-dimensional (2D) layer. While in a kagome lattice, the triangles are corner shared in a 2D layer which amplifies the degree of frustration compared to an edge shared triangular lattice. In perfect low spin ($S = \frac{1}{2}$) kagome lattice antiferromagnets (KLAFs), quantum fluctuations along with strong magnetic frustration impede conventional magnetic LRO and give rise to a strongly correlated QSL or other nontrivial ground states [4]. A celebrated example is herbertsmithite $ZnCu_3(OH)_6Cl_2$, which is the first realization of a perfect $S = \frac{1}{2}$ kagome compound with no magnetic LRO down to 50 mK, confirming QSL [5–7].

Several phase diagrams have been reported theoretically for KLAFs, predicting a large variety of ground states as a function of the ratio of exchange couplings and also applied magnetic field [8–10]. Experimentally, many compounds have been discovered and investigated which either show a subtle deviation from ideal 2D kagome geometry or are having strong anisotropy, leading to magnetic LRO and/or other exotic phases at finite temperatures [11]. Apart from perfect kagome lattice, many special derivatives of kagome lattice have also been discovered that include square kagome [12], octa-kagome [13], staircase kagome [14,15], sphere kagome [16], strip kagome [17,18], tripod kagome [19,20], hyperkagome [21,22], etc. Because of a more intricate lattice geometry, these derivatives harbor an array of intriguing magnetic ground states. To name a few, QSL is realized in the square-kagome compound $KCu_6AlBiO_4(SO_4)_5Cl$ [12] and hyperkagome compound $Na_4Ir_3O_8$ [21], and spin-singlet and antiferromagnetic ordering are observed in octa-kagome lattices $BiOCu_2(Te, Se)O_3(SO_4)(OH) \cdot H_2O$, respectively [13], a spin-ice-type ground state is reported in the tripod-kagome lattice $Mg_2Dy_3Sb_3O_{14}$ [19], etc.

Recently, a new kagome variant, a capped-kagome lattice compound with the general formula $(MX)Cu_5O_2(T^{5+}O_4)_2$ ($M$ = K, Rb, Cs, Cu; $X$ = Cl, Br; $T^{5+}$ = P, V) is being pursued rigorously. This series belongs to the averievite family, an oxide mineral found as a product of posteruption volcanic activity. Most of these compounds show a structural transition from a high symmetric trigonal at high temperatures to a low symmetric monoclinic phase at low temperatures. In this series, the magnetic properties of the only compound $(CsCl)Cu_5V_2O_{10}$ (CCCVO) are elaborately studied, which undergoes a structural transition at 310 K [23,24]. Magnetic susceptibility reveals a large Curie-Weiss (CW) temperature $\theta_{CW} \simeq -185$ K and the compound encounters a magnetic LRO at around $T_N \simeq 24$ K. $Zn^{2+}$ substitution at the capped $Cu^{2+}$ site [i.e., $(CsCl)Cu_{5-x}Zn_xV_2O_{10}$] suppresses the magnetic as well as the structural transitions and is expected to yield QSL for $x = 2$ [25,26]. Some preliminary magnetic

*rnath@iisertvm.ac.in

 

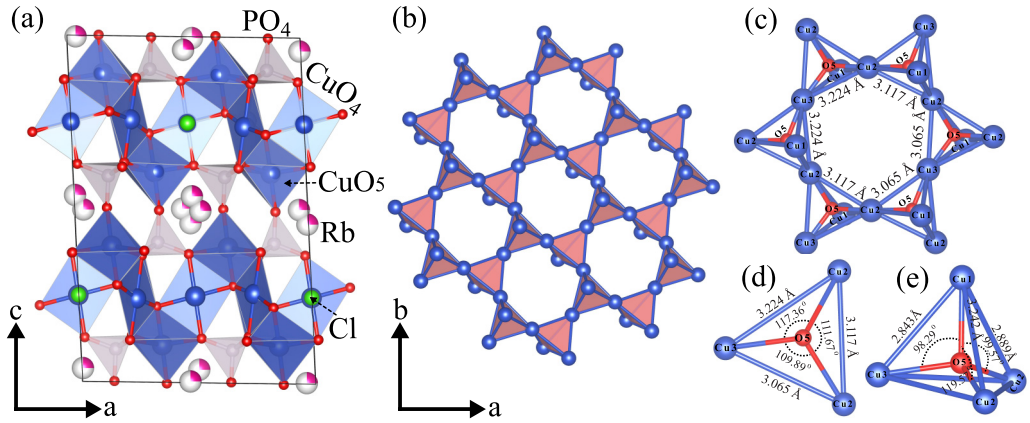


FIG. 1. (a) Crystal structure of $(RbCl)Cu_5P_2O_{10}$ projected in the *ac* plane. The connection of $Cu(2,3)O_4$ square planes (plaquettes) and $Cu(1)O_5$ square pyramids forming capped-kagome layers. $PO_4$ tetrahedra are connecting these layers along the *c* direction. (b) A section of the capped-kagome layer in the *ab* plane. (c) A hexagonal ring showing the bond lengths. (d) Triangular base of the $OCu_4$ tetrahedron with bond lengths and bond angles. (e) The bond lengths and bond angles of the apical Cu atom with basal Cu atoms of the $OCu_4$ tetrahedron.

data are also reported for the phosphate analog compounds $(CsCl, CsBr, CsI)Cu_5P_2O_{10}$ [27]. Recently, two more new capped-kagome compounds (molybdate tellurites) based on $Ni^{2+}$ and $Cu^{2+}$ are also reported [28]. Thus, the interesting structural aspects and highly frustrated geometry make these compounds very special in the context of new quantum phase transitions.

In this paper, we carried out a comprehensive study of the structural and magnetic properties of a phosphate averievite $(RbCl)Cu_5P_2O_{10}$, abbreviated as RCCPO. RCCPO is reported to crystallize in a monoclinic structure with space group $C2/c$ (No. 15) at room temperature [29]. The crystal structure illustrated in Fig. 1 consists of capped-kagome layers, made up of corner sharing anion-centered $OCu_4$ tetrahedral units, arranged in an up-down-up-down fashion [see Fig. 1(b)]. There are three inequivalent Cu sites in the formula unit. Two Cu sites (Cu2 and Cu3) possess distorted $CuO_4$ square planar geometry while the Cu1 site forms a distorted $CuO_5$ square pyramid. The $CuO_4$ squares share corners in order to make the kagome plane and the $CuO_5$ square pyramids share the edges with the adjacent $CuO_4$ squares that form the $OCu_4$ tetrahedra units and hence the capped-kagome network. Here, O5 is the common oxygen that provides the interaction path among two Cu2 and one Cu3 ions at the triangular base and the apical Cu1 ion in an anion-centered $OCu_4$ tetrahedron. The $Cl^-$ ions are located at the center of the hexagonal rings while the $Rb^+$ ions are located in the interlayer spacing. The nonmagnetic $PO_4$ tetrahedra are placed between the capped-kagome layers and connect the capped $Cu^{2+}$ of one layer with $Cu^{2+}$ ions of the neighboring layers. This provides three-dimensional (3D) coupling along the *c* direction [see Fig. 1(a)]. Further, owing to the low symmetry crystal structure, the $Cu^{2+}$-$Cu^{2+}$ distances within each $OCu_4$ tetrahedral unit are unequal, which induces distortion in the capped-kagome layer [see Figs. 1(c)–1(e)]. All these effects render the spin lattice more complex, opening up the possibility of observing nontrivial ground states. Our magnetic measurements reveal that RCCPO is a highly frustrated magnet and it undergoes two consecutive magnetic transitions at low temperatures.

## II. EXPERIMENTAL DETAILS

A polycrystalline sample of RCCPO was synthesized by the conventional solid-state reaction technique. The synthesis involves two steps. In the first step, the precursor $Cu_2P_2O_7$ was prepared by heating the stoichiometric mixture of CuO (Aldrich, 99.999%) and $NH_2H_2PO_4$ (Aldrich, 99.999%). These reagents were finely ground, pressed into pellets, and prereacted in air at 350 °C for 12 h in order to remove ammonia and water. The obtained soft pellets were ground again, sealed in an evacuated quartz tube, and heated at 800 °C for 24 h. In the second step, the obtained $Cu_2P_2O_7$ powder was mixed in a stoichiometric ratio with CuO (Aldrich, 99.999%) and RbCl (Aldrich, 99.999%), ground, pelletized, sealed in an evacuated quartz tube, and annealed at 550–570 °C with multiple intermediate regrindings. The phase purity of the product was confirmed by powder x-ray diffraction (XRD) recorded at room temperature using a PANalytical x-ray diffractometer ($CuK\alpha$ radiation, $\lambda_{avg} \simeq 1.5418$ Å). To check if any structural transition is present, temperature-dependent powder XRD was performed over a broad temperature range ($13\ K \leqslant T \leqslant 400\ K$). For low-temperature measurements, a low-$T$ attachment (Oxford Phenix), and for high-temperature measurements, a high-$T$ oven attachment (Anton-Paar HTK 1200N) to the x-ray diffractometer were used. Rietveld refinement of the powder XRD was performed using the FULLPROF software package [30], taking the initial structural parameters from the previous report [29].

The dc magnetization ($M$) was measured as a function of temperature ($1.9\ K \leqslant T \leqslant 380\ K$) in different magnetic fields, using the vibrating sample magnetometer (VSM) attachment to the physical property measurement system [(PPMS) Quantum Design]. Similarly, ac susceptibility was measured as a function of temperature ($1.9\ K \leqslant T \leqslant 100\ K$) and frequency ($200\ Hz \leqslant \nu \leqslant 10\ kHz$) in an ac field of 10 Oe using the ACMS option of the PPMS. Heat capacity ($C_p$) as a function of $T$ and $H$ was measured on a small piece of sintered pellet using the thermal relaxation technique in PPMS.

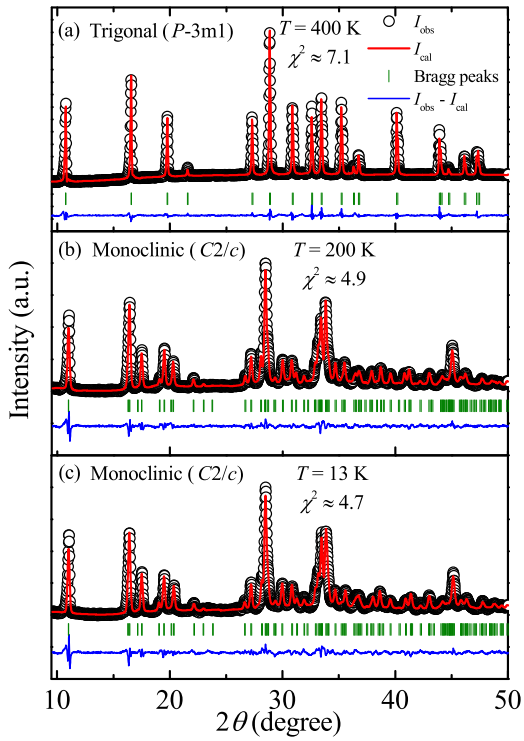


FIG. 2. Powder XRD patterns (open circles) at (a) 400 K, (b) 200 K, and (c) 13 K. The solid lines denote the Rietveld refinement of the data. The Bragg peak positions are indicated by green vertical bars and the bottom solid line indicates the difference between the experimental and calculated intensities. The crystal structure and the corresponding space group at different temperatures are also indicated.

Nuclear magnetic resonance (NMR) measurements were carried out using a laboratory-built phase-coherent spin-echo pulse spectrometer on the $^{31}$P nuclei (nuclear spin $I = \frac{1}{2}$ and gyromagnetic ratio $\gamma_N/2\pi = 17.237$ MHz/T). We performed the experiments at two radio frequencies ($f =$ 49.6 and 120.6 MHz) and over a wide temperature range (1.8 K $\leqslant T \leqslant$ 300 K). The $^{31}$P NMR spectra were obtained by sweeping the magnetic field, keeping the frequency fixed. The temperature-dependent NMR shift $K(T) = [H_{\rm ref} - H(T)]/H(T)$ was calculated by taking the resonance field of the sample ($H$) with respect to the resonance field of a nonmagnetic reference ($H_{\rm ref}$) $H_3PO_4$. The $^{31}$P spin-lattice relaxation rate ($1/T_1$) was measured by the standard saturation recovery method. The $^{31}$P spin-spin relaxation rate ($1/T_2$) was obtained by measuring the decay of the echo integral with variable spacing between the $\pi/2$ and $\pi$ pulses.

## III. RESULTS

### A. X-ray diffraction

In order to detect the structural transition or lattice distortion, if any, powder XRD was measured at different intermediate temperatures from 13 to 400 K. Figure 2 displays the powder XRD patterns of RCCPO at 400, 200, and 13 K along with the Rietveld fit. At room temperature (300 K), all the diffraction peaks can be well indexed to the monoclinic unit cell with $C2/c$ symmetry. The obtained lattice parameters at room temperature are $a = 10.868(4)$ Å, $b = 6.207(5)$ Å, $c = 16.181(5)$ Å, $\beta = 93.391(3)^\circ$, and the unit cell volume $V_{\rm cell} \simeq 1089.621$ Å$^3$, which are in close agreement with the previous report [29]. The absence of any visible change in the XRD pattern down to 13 K indicates no structural distortion from 300 down to 13 K. However, a change in the diffraction pattern was observed above $T_{\rm t} \sim 310$ K with the splitting of certain Bragg peaks and the appearance of new peaks. Above ~340 K, the XRD pattern completely stabilizes in a more symmetric crystal structure with a fewer number of Bragg peaks compare to the room-temperature crystal structure. The analysis of the XRD pattern at 400 K confirmed a trigonal structure with space group $P\bar{3}m1$ (No. 164). The refined lattice parameters are $a = 6.185(4)$ Å, $c = 8.241(5)$ Å, and $V_{\rm cell} \simeq$ 273.1 Å$^3$. Thus, a structural transition occurs at around 310 K from the high-temperature trigonal to low-temperature monoclinic structure, similar to the analog compound CCCVO. In an intermediate-temperature regime around 300 K both phases coexist and the data could be fitted using two phases. The obtained atomic parameters at 400 K (trigonal) and 200 K (monoclinic) are listed in Tables I and II, respectively.

TABLE I. Structural parameters of RCCPO obtained from the Rietveld refinement of the powder XRD data at 400 K [trigonal, space group: $P\bar{3}m1$ (No. 164)]. Our fit yields $a = 6.185(4)$ Å, $c = 8.241(5)$ Å, $V_{\rm cell} \simeq 273.1$ Å$^3$, $R_{\rm p} \simeq 14.5$, and $\chi^2 = (\frac{R_{\rm wp}}{R_{\rm exp}})^2 \simeq 7.2$. Listed are the Wyckoff positions and the refined atomic coordinates for each atom.

| Atom | Wyckoff | $x$ | $y$ | $z$ | Occ. |
|---|---|---|---|---|---|
| Rb1 | 1$a$ | 1.000 | 1.000 | 1.000 | 0.60 |
| Rb2 | 2$c$ | 1.000 | 1.000 | 0.877(3) | 0.20 |
| Cl1 | 1$b$ | 1.000 | 1.000 | 0.500 | 1.00 |
| Cu1 | 2$d$ | 0.333 | 0.666 | 0.210(1) | 1.00 |
| Cu2 | 3$f$ | 0.000 | 0.500 | 0.500 | 1.00 |
| P1 | 2$d$ | 0.333 | 0.666 | 0.800(2) | 1.00 |
| O1 | 2$d$ | 0.333 | 0.666 | 1.014(1) | 1.00 |
| O2 | 6$i$ | 0.061(3) | 0.530(1) | 0.752(4) | 1.00 |
| O3 | 2$d$ | 0.333 | 0.666 | 0.452(1) | 1.00 |

The temperature evolution of lattice parameters from 13 to 400 K is presented in Fig. 3. As shown in Fig. 3(a), associated with the symmetry lowering, the in-plane and out-of-plane lattice constants transform into $a_{\rm m} \simeq \sqrt{3}a_{\rm t}$, $b_{\rm m} \simeq b_{\rm t}$, and $c_{\rm m} \simeq 2c_{\rm t}$, respectively [31,32]. Here, the subscripts m and t denote the monoclinic and trigonal structures, respectively. Figure 3(b) presents the temperature variation of angle ($\beta$) and $V_{\rm cell}$ from 13 to 300 K in the monoclinic phase. $\beta$ increases with decreasing temperature but $V_{\rm cell}$ is found to decrease systematically upon cooling. The variation of $V_{\rm cell}$ with temperature can be expressed in terms of the internal energy [$U(T)$] of the system [33]

$$V_{\rm cell}(T) = \frac{\gamma U(T)}{K_0} + V_0, \tag{1}$$

where $V_0$ is the cell volume at $T = 0$ K, $K_0$ is the bulk modulus of the system, and $\gamma$ is the Grüneisen parameter. $U(T)$ is the internal energy which can be expressed in terms of the Debye

TABLE II. Structural parameters of RCCPO obtained from the Rietveld refinement of the powder XRD data at 200 K [monoclinic, space group: $C2/c$ (No. 15)]. Our fit yields $a = 10.860(4)$ Å, $b = 6.221(5)$ Å, $c = 16.130(5)$ Å, $\beta = 93.724(3)^\circ$, $V_{\text{cell}} \simeq 1087.44$ Å$^3$, $R_{\text{p}} \simeq 14.8$, and $\chi^2 = (\frac{R_{\text{wp}}}{R_{\text{exp}}})^2 \simeq 4.9$. Listed are the Wyckoff positions and the refined atomic coordinates for each atom.

| Atom | Wyckoff | $x$ | $y$ | $z$ | Occ. |
|---|---|---|---|---|---|
| Rb1 | 8$f$ | 0.506(2) | 0.028(2) | 0.546(2) | 0.25 |
| Rb2 | 8$f$ | 0.471(2) | 0.033(2) | 0.506(2) | 0.25 |
| Cl1 | 4$e$ | 0.500 | 1.065(1) | 0.750 | 1.00 |
| Cu1 | 8$f$ | 0.346(2) | 0.472(3) | 0.606(1) | 1.00 |
| Cu2 | 8$f$ | 0.242(2) | 0.807(2) | 0.741(2) | 1.00 |
| Cu3 | 4$e$ | 0.500 | 0.606(2) | 0.750 | 1.00 |
| P1 | 8$f$ | 0.350(2) | 0.436(1) | 0.403(2) | 1.00 |
| O1 | 8$f$ | 0.488(2) | 0.421(2) | 0.379(1) | 1.00 |
| O2 | 8$f$ | 0.281(1) | 0.226(1) | 0.382(1) | 1.00 |
| O3 | 8$f$ | 0.283(2) | 0.642(2) | 0.381(2) | 1.00 |
| O4 | 8$f$ | 0.358(2) | 0.384(2) | 0.497(2) | 1.00 |
| O5 | 8$f$ | 0.327(2) | 0.544(2) | 0.720(2) | 1.00 |

approximation [34] as

$$U(T) = 9Nk_{\text{B}}T\left(\frac{T}{\theta_{\text{D}}}\right)^3 \int_0^{\frac{\theta_{\text{D}}}{T}} \frac{x^3}{(e^x - 1)} dx. \quad (2)$$

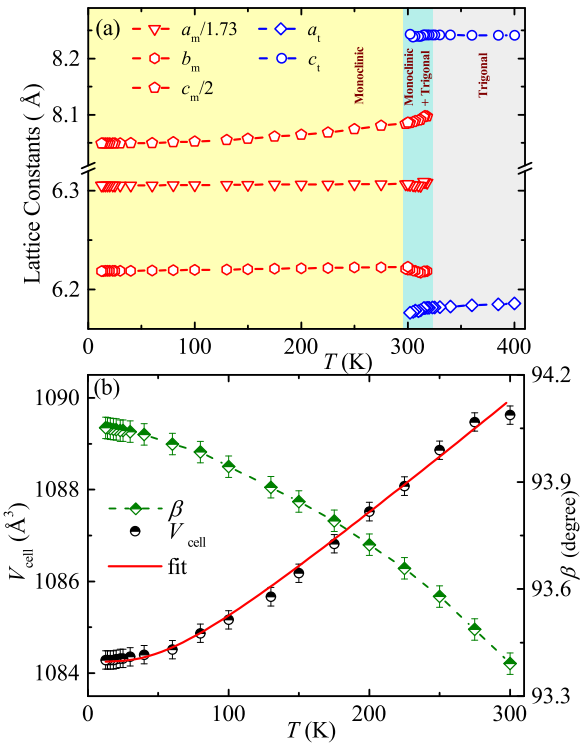


FIG. 3. (a) Lattice constants ($a$, $b$, and $c$) as a function of temperature from 13 to 400 K. The lattice constants in the monoclinic phase are scaled with respect to the high symmetry trigonal structure. The areas shaded in yellow, gray, and cyan colors represent the regimes for pure monoclinic, trigonal, and the coexistence of both phases, respectively. (b) Monoclinic angle ($\beta$) and the unit cell volume ($V_{\text{cell}}$) as a function of temperature from 13 to 300 K. The solid line represents the fit of $V_{\text{cell}}(T)$ using Eq. (1).

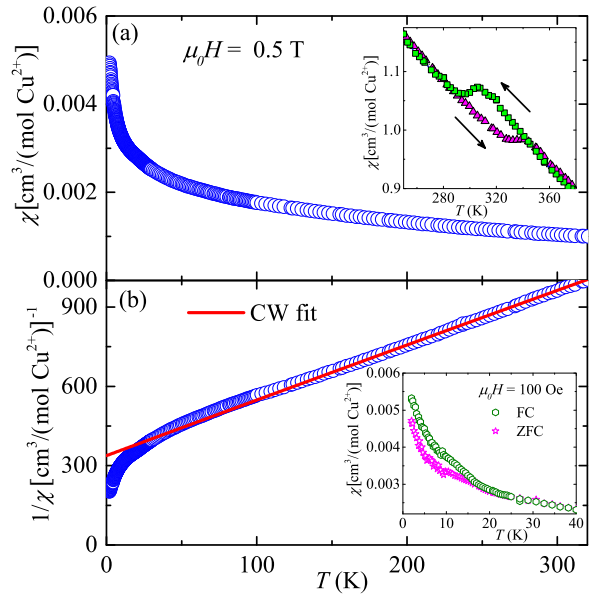


FIG. 4. (a) Temperature-dependent dc susceptibility $\chi(T)$ measured at an applied field of $\mu_0 H = 0.5$ T. Inset: Thermal hysteresis around the structural transition measured under FCW and FCC conditions. (b) Inverse susceptibility ($1/\chi$) vs $T$ at $\mu_0 H = 0.5$ T and the solid line is the CW fit for 200 K $\leqslant T \leqslant$ 300 K, below the structural transition. Inset: $\chi(T)$ measured at $H = 100$ Oe in ZFC and FC protocols.

Here, $N$ is the number of atoms in the unit cell, $k_{\text{B}}$ is the Boltzmann constant, and $\theta_{\text{D}}$ is the Debye temperature. The variable $x$ inside the integration stands for the quantity $\frac{\hbar\omega}{k_{\text{B}}T}$ with phonon frequency $\omega$ and Planck constant $\hbar$. Here, $\theta_{\text{D}} = \frac{\hbar\omega_{\text{D}}}{k_{\text{B}}}$ and $\omega_{\text{D}}$ is the upper limit of $\omega$. The best fit of the $V_{\text{cell}}(T)$ data using Eq. (1) [solid line in Fig. 3(b)] yields the parameters $\theta_{\text{D}} \simeq 225$ K, $V_0 \simeq 1084.25$ Å$^3$, and $\frac{\gamma}{K_0} \simeq 8.08 \times 10^{-12}$ Pa$^{-1}$.

### B. Magnetization

The temperature-dependent dc susceptibility $\chi(T)$ ($\equiv M/H$) of the polycrystalline RCCPO sample measured in an applied field of $\mu_0 H = 0.5$ T is shown in the Fig. 4(a). At high temperatures, $\chi(T)$ increases with decreasing temperature in a Curie-Weiss (CW) manner as expected in the paramagnetic regime. No clear indication of any magnetic LRO is detected down to 2 K. $\chi(T)$ measured under field-cooled-warming (FCW) and field-cooled-cooling (FCC) conditions shows a clear thermal hysteresis [inset of Fig. 4(a)] confirming the structural phase transition.

Figure 4(b) shows the inverse magnetic susceptibility $1/\chi(T)$ for $\mu_0 H = 0.5$ T. In the paramagnetic regime $1/\chi(T)$ typically shows a linear behavior with temperature, due to uncorrelated moments. To extract the magnetic parameters, $1/\chi(T)$ was fitted in the temperature range 200 K $\leqslant T \leqslant$ 300 K below the structural transition by the CW law

$$\chi(T) = \chi_0 + \frac{C}{T - \theta_{\text{CW}}}, \quad (3)$$

where $\chi_0$ is the temperature-independent susceptibility, which includes Van Vleck paramagnetism and core diamagnetism. The second term is the CW law where $C$ is the Curie

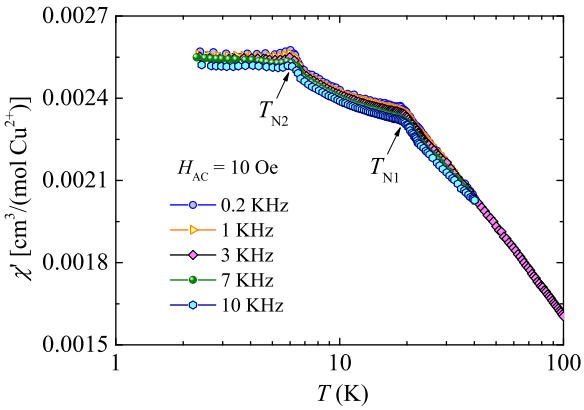


FIG. 5. Real part of ac susceptibility $\chi'$ vs $T$ at different frequencies. The arrows point to the magnetic anomalies.

constant and $\theta_{CW}$ is the CW temperature. The fit yields $\chi_0 \simeq 2.19 \times 10^{-4}$ cm$^3$/mol-Cu$^{2+}$, $C \simeq 0.46$ cm$^3$ K/(mol-Cu$^{2+}$), and $\theta_{CW} \simeq -160$ K. The large negative value of $\theta_{CW}$ suggests that the dominant exchange interactions between $Cu^{2+}$ ions are antiferromagnetic (AFM) in nature. From the value of $C$, the effective moment is calculated to be $\mu_{eff} \simeq 1.93\mu_B/Cu^{2+}$using the relation $\mu_{eff} = \sqrt{3k_BC/N_A\mu_B^2}$, where $N_A$ is the Avogadro's number and $\mu_B$ is the Bohr magneton. For a spin-$\frac{1}{2}$ system, the spin-only effective moment is expected to be $\mu_{eff} = g\sqrt{S(S+1)}\mu_B \simeq 1.73\mu_B$, assuming a Landé $g$-factor $g \simeq 2$. However, our experimental value of $\mu_{eff} \simeq 1.93\mu_B/Cu^{2+}$ is slightly higher than the spin-only value and corresponds to $g \simeq 2.22$. Such a large value of $g$ is typically observed for powder samples containing a magnetic $Cu^{2+}$ ion [35]. The core diamagnetic susceptibility $\chi_{core}$ of RCCPO is calculated to be $-2.22 \times 10^{-4}$ cm$^3$/mol by adding the core diamagnetic susceptibilities of the individual ions $Rb^+$, $Cl^-$, $Cu^{2+}$, $P^{5+}$, and $O^{2-}$ [36]. The Van Vleck paramagnetic susceptibility ($\chi_{VV}$) is estimated by subtracting $\chi_{dia}$ from $\chi_0$ to be $\sim 4.41 \times 10^{-4}$ cm$^3$/mol. This value of $\chi_{VV}$ is close to the values reported for other cuprates [37,38].

As depicted in the inset of Fig. 4(b), the zero-field-cooled (ZFC) and field-cooled (FC) susceptibilities in $H = 100$ Oe show a weak splitting at $T_{N1} \simeq 20$ K, indicating either the onset of a magnetic LRO or a spin-glass (SG) transition. The extent of frustration in a spin system can be quantified by the frustration ratio $f = \frac{|\theta_{CW}|}{T_{N1}}$. According to the mean-field theory, $\theta_{CW}$ is the sum of all exchange interactions present in the system. Typically, for a nonfrustrated AFM system, $f$ is close to 1. However, for a highly frustrated AFM, the $f$ value is much larger than 1. For RCCPO, the frustration ratio is calculated to be $f \simeq 160/20 \simeq 8$ which corroborates the strong frustration in the system.

Figure 5 presents the temperature-dependent ac susceptibility measured in different frequencies and at a fixed ac field of $H_{ac} \simeq 10$ Oe. In contrast to dc $\chi(T)$, the real part of the ac susceptibility $\chi'(T)$ shows two anomalies at $T_{N1} \simeq 20$ K and $T_{N2} \simeq 7$ K, reflecting two magnetic transitions. The peak at $T_{N1} \simeq 20$ K is found to be weakly frequency dependent, which shifts towards higher temperatures with increasing frequency. This is a possible indication of canted antiferromagnetism or

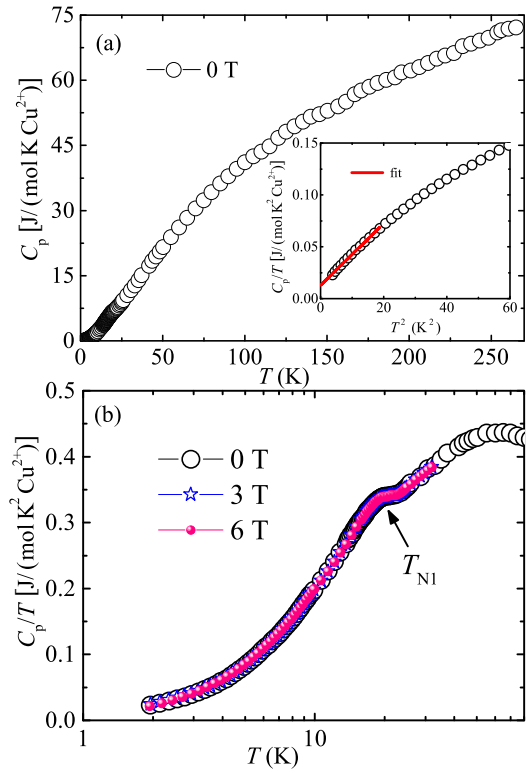


FIG. 6. (a) $C_p(T)$ of RCCPO measured in zero field. Inset: $C_p/T$ vs $T^2$ in zero field, showing the linear regime below $T_{N2}$. The solid line is the linear fit. (b) $C_p/T$ vs $T$ measured in different applied fields in the low-temperature region, around $T_{N1}$.

a SG-type transition. On the other hand, the peak at $T_{N2} \simeq 7$ K is found to be frequency independent, suggesting the onset of a robust AFM LRO.

### C. Heat capacity

Temperature-dependent heat capacity $C_p(T)$ measured in zero field is presented in Fig. 6(a). At high temperatures, $C_p$ is dominated by the phonon excitations while at low temperatures it is dominated by the magnetic contribution. As the temperature is lowered, $C_p$ shows a weak cusp at $T_{N1} \simeq 20$ K [see Fig. 6(b)]. The position of this cusp is unaffected by the external magnetic field up to 6 T. However, no obvious feature is evident at $T_{N2} \simeq 7$ K, likely due to a weak entropy change across $T_{N2}$. Below 4 K, the spin-wave dispersion gives rise to a $T^3$ behavior, as expected in a 3D AFM ordered state [38]. The plot of $C_p/T$ vs $T^2$ in the inset of Fig. 6(a) highlights the linear behavior below 4 K. Moreover, in case of a SG transition, $C_p(T)$ at low temperatures deviates from the $T^3$ behavior and is usually described by $C_p(T) = \beta T^3 + \delta T^{3/2}$ [39]. Thus, only the $T^3$ dependence of $C_p(T)$ also rules out a SG transition at $T_{N2}$ and establishes the canted-AFM nature of the transition. Due to the unavailability of a suitable nonmagnetic analog, we are unable to separate the magnetic part of the heat capacity from the total $C_p(T)$.

### D. $^{31}$P NMR

NMR is an immensely powerful local tool to study the static and dynamic properties of a spin system. The crystal

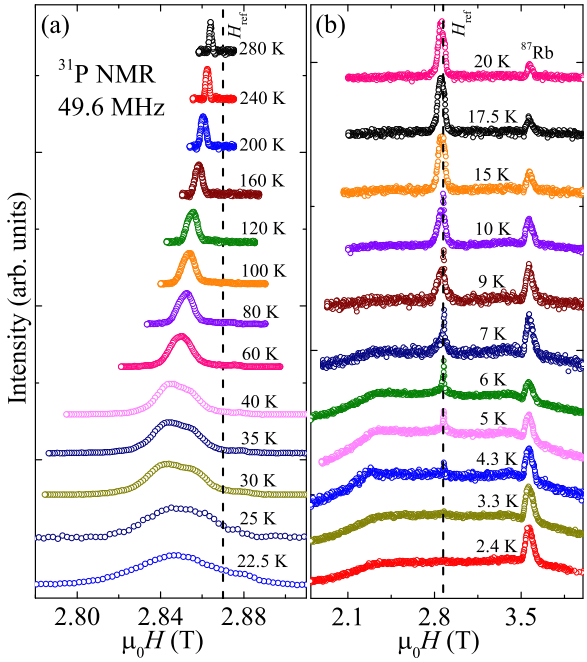


FIG. 7. (a) Temperature evolution of $^{31}$P NMR spectra measured at a radio frequency $f = 49.6$ MHz, above $T_{N1}$. The vertical dashed line corresponds to the $^{31}$P nonmagnetic reference field position. (b) $^{31}$P NMR spectra below $T_{N1}$. The peak at the right side corresponds to the signal of $^{87}$Rb present in the sample.

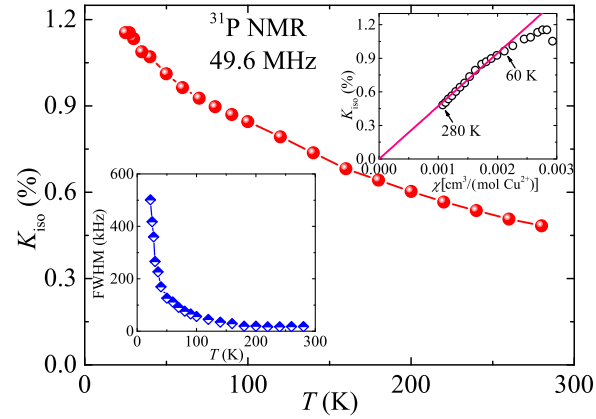


FIG. 8. Temperature-dependent $^{31}$P NMR isoshift $K_{iso}$ measured at 49.6 MHz. Upper inset: $K_{iso}$ vs $\chi$ (measured at 3 T). The solid line is the straight line fit. Lower inset: Full width at half maximum (FWHM) vs $T$.

structure of RCCPO has a unique $^{31}$P site. Two adjacent capped-kagome layers in the *ac* plane are connected through the $PO_4$ tetrahedra. Since $^{31}$P is coupled with the $Cu^{2+}$ ions, through $^{31}$P NMR, one can probe the static and dynamic properties of $Cu^{2+}$ spins.

### *1.* $^{31}$P *NMR spectra*

The field-sweep $^{31}$P NMR spectra measured at different temperatures (2.4 K $\leqslant T \leqslant$ 280 K) at a radio frequency of 49.6 MHz are shown in Fig. 7. Each NMR spectrum is normalized by its maximum amplitude and offset vertically by adding a constant. The spectral line consists of a single spectral line, typical for $I = 1/2$ nuclei [40]. The spectral line is symmetric at high temperatures and becomes asymmetric as we go down in temperature. Since our measurements are done on a randomly oriented polycrystalline sample, the asymmetric shape of the spectra can be attributed to a powder pattern due to an asymmetric hyperfine coupling constant and/or an anisotropic susceptibility [41]. With decreasing temperature, the line broadens and the peak position shifts with temperature. The NMR shift $K(T)$ is the direct measure of intrinsic spin susceptibility $\chi_{spin}(T)$ and is free from extrinsic contributions. Therefore, one can write $K(T)$ in terms of $\chi_{spin}(T)$ as

$$K(T) = K_0 + \frac{A_{hf}}{N_A}\chi_{spin}(T), \tag{4}$$

where $K_0$ is the temperature-independent chemical shift and $A_{hf}$ is the hyperfine coupling constant between the $^{31}$P nuclei and $Cu^{2+}$ electronic spins. The isotropic NMR shift $K_{iso}$ obtained by fitting the NMR spectra is plotted as a function of $T$ in Fig. 8. The upper inset of Fig. 8 shows the $K_{iso}$ vs $\chi$ plot with $T$ as an implicit parameter. A straight line fit over a temperature range 60 K $\leqslant T \leqslant$ 280 K yields the isotropic part of the hyperfine coupling $A_{iso} \simeq 2.93$ T/$\mu_B$. The small deviation from linearity below 60 K can be attributed to a small amount of paramagnetic impurities to which $K_{iso}$ is insensitive. The full width at half maximum (FWHM) obtained from the spectral fit is plotted against $T$ in the lower inset of Fig. 8. It increases with lowering temperature and then shoots up below about 30 K, which suggests the growth of internal field as we approach the magnetic ordering at $T_{N1}$.

Figure 7(b) presents $^{31}$P NMR spectra below $T_{N1}$. Below about 22 K, the NMR line broadens drastically, implying that $^{31}$P senses the internal field in the ordered state. The spectrum seems to form a triangular line shape, typically expected for a powder sample in an incommensurate spin-density-wave state [42–45]. Below the second transition $T_{N2} \simeq 9.5$ K, a huge internal field pops up, leading to a drastic line broadening, and the line attains a nearly rectangular shape superimposed with a sharp line at the center of gravity $H \simeq 2.87$ T, which is the zero-shift resonance position of $^{31}$P nuclei. With decreasing temperature, this line broadening increases and the intensity of the central narrow line decreases. This rectangular line shape is reminiscent of a commensurate AFM ordering [44–47]. An additional signal appears at low temperatures which overlaps with the right shoulder of the rectangular pattern. This peak position is almost temperature independent and corresponds to the signal of $^{87}$Rb present in the sample.

### *2. Spin-lattice relaxation rate* $1/T_1$

To understand the local spin-spin correlation, the $^{31}$P spin-lattice relaxation rate $1/T_1$ was measured as a function of temperature down to 2.4 K at the central peak position and at two different frequencies, 49.6 and 120.6 MHz. For an $I = 1/2$ nucleus, the recovery of the longitudinal magnetization is expected to follow a single exponential behavior. Indeed, our recovery curves were fitted well by the stretched exponential

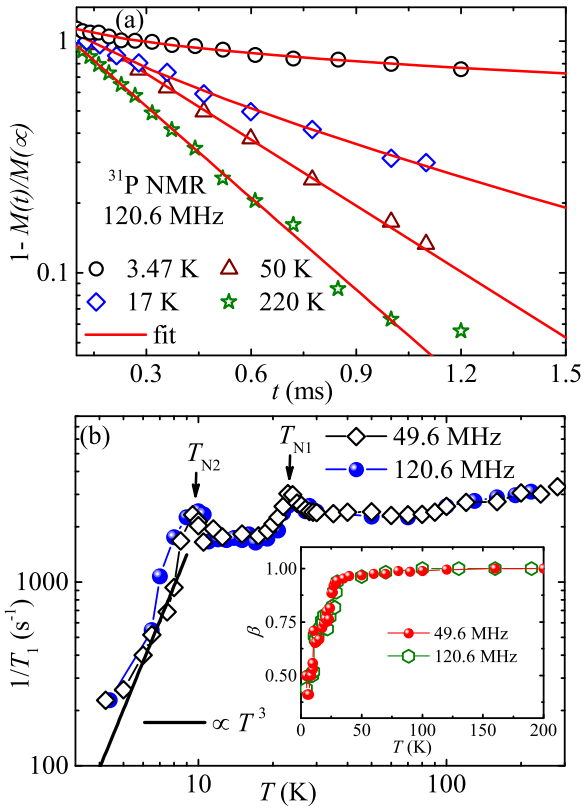


FIG. 9. (a) Longitudinal magnetization recovery curves for 120.6 MHz at four selective temperatures measured on the $^{31}$P nuclei and the solid lines are fits using Eq. (5). (b) $^{31}$P NMR spin-lattice relaxation rate ($1/T_1$) vs $T$ measured at 49.6 and 120.6 MHz. The downward arrows point to $T_{N1} \simeq 23.5$ K and $T_{N2} \simeq 9.5$ K. The solid line represents $T^3$ behavior below $T_{N2}$. Inset: Exponent $\beta$ as a function of $T$ for both the frequencies.

function

$$1 - \frac{M(t)}{M(\infty)} = Ae^{-(t/T_1)^{\beta}}, \tag{5}$$

where $M(t)$ is the nuclear magnetization at a time $t$ after the saturation pulse, $M(\infty)$ is the equilibrium nuclear magnetization, and $\beta$ is the stretch exponent. Recovery curves for 120.6 MHz in four different temperatures along with the fits are shown in Fig. 9(a).

The temperature dependence of $1/T_1$ extracted following the above fitting procedure is presented in Fig. 9(b) for both frequencies. The exponent $\beta$ as a function of $T$ for both frequencies is also plotted in the inset of Fig. 9(b). At high temperatures ($T > 30$ K), the value of $\beta$ is found to be close to 1 and is almost temperature independent, suggesting a uniform relaxation process in this temperature range. However, a drastic drop in the $\beta$ value below about 25 K indicates the distribution of relaxation time in the ordered state which is possibly due to some kind of disorder at the magnetic sites [48]. Similarly, $1/T_1$ in the high-temperature regime ($T > 75$ K) is almost temperature independent due to localized moments in the paramagnetic state [49]. At low temperatures, $1/T_1$ exhibits two sharp peaks at around $T_{N1} \simeq 23.5$ K and $T_{N2} \simeq 9.5$ K, indicating the slowing down of fluctuating moments as we approach the magnetic transitions. These findings corroborate the double transitions observed from the ac susceptibility measurements. Note that the transition anomalies in $1/T_1$ appear at slightly higher temperatures compared to that observed in ac susceptibility data, which is due to the different thermocouples with different calibrations used in the NMR and PPMS cryostats. Below $T_{N2}$, $1/T_1$ drops swiftly toward zero because of the release of critical fluctuations and the scattering of magnons by the nuclear spins [50–52]. For $T \gg \Delta/k_B$, $1/T_1$ follows either a $T^3$ behavior or a $T^5$ behavior due to a two-magnon Raman process or a three-magnon process, respectively, where $\Delta/k_B$ is the energy gap in the spin-wave excitation spectrum [50]. On the other hand, for $T \ll \Delta/k_B$, it follows an activated behavior $1/T_1 \propto T^2 e^{-\Delta/k_B T}$. As shown in Fig. 9(b), $1/T_1$ below $T_{N2}$ follows a nearly $T^3$ behavior, ascertaining that the relaxation is mainly governed by a two magnon process similar to that reported for other frustrated magnets [52].

From the constant value of $1/T_1$ at high temperatures, one can estimate the leading exchange coupling between $Cu^{2+}$ ions, using the hyperfine coupling between P and Cu atoms. At high temperatures, $1/T_1$ can be expressed as [49,52]

$$\left(\frac{1}{T_1}\right)_{T\to\infty} = \frac{(\gamma_N g \mu_B)^2 \sqrt{2\pi} z' S(S+1)}{3\,\omega_{ex}} \left(\frac{A_z}{z'}\right)^2, \tag{6}$$

where $\omega_{ex} = (|J^{max}|k_B/\hbar)\sqrt{2zS(S+1)/3}$ is the Heisenberg exchange frequency, $z$ is the number of nearest-neighbor spins of each $Cu^{2+}$ ion, and $z'$ is the number of nearest-neighbor $Cu^{2+}$ spins attached to a given P site. In RCCPO, each $Cu^{2+}$ ion in the kagome plane has six nearest neighbors while each capped $Cu^{2+}$ ion can see only three neighboring ions. Therefore, on an average each $Cu^{2+}$ spin sees 4.5 neighboring spins. Similarly, each P site is strongly connected to five nearest-neighbor $Cu^{2+}$ spins. Thus, using the parameters $A_z \simeq 2.93$ T/$\mu_B$, $\gamma_N = 108.303 \times 10^2$ rad s$^{-1}$ Oe$^{-1}$, $z = 4.5$, $z' = 5$, $g = 2.22$, $S = \frac{1}{2}$, and the relaxation rate at 160 K of $(\frac{1}{T_1})_{T\to\infty} \simeq 2714.7$ s$^{-1}$, the magnitude of the leading antiferromagnetic exchange coupling is calculated to be $J^{max}/k_B \simeq 117$ K.

### 3. *Spin-spin relaxation rate* $1/T_2$

In order to measure the spin-spin relaxation rate $1/T_2$, the decay of the transverse magnetization ($M_{xy}$) was monitored after a $\pi/2$-$\tau$-$\pi$ pulse sequence as a function of the pulse separation time $\tau$. The recovery curves are then fitted by the following equation,

$$M_{xy} = M_0 e^{-(2\tau/T_2)}. \tag{7}$$

Recovery curves at a few selected temperatures along with the fits are depicted in Fig. 10(a). The extracted $1/T_2$ is plotted as a function of temperature in Fig. 10(b). Similar to $1/T_1$, $1/T_2$ also exhibits two sharp peaks, further establishing double transitions at $T_{N1} \simeq 23.5$ K and $T_{N2} \simeq 9.5$ K.

## IV. DISCUSSION AND SUMMARY

This averievite family of compounds is an interesting class of compounds where the replacement of any ion in the structure affects the geometry of the $OCu_4$ tetrahedron and

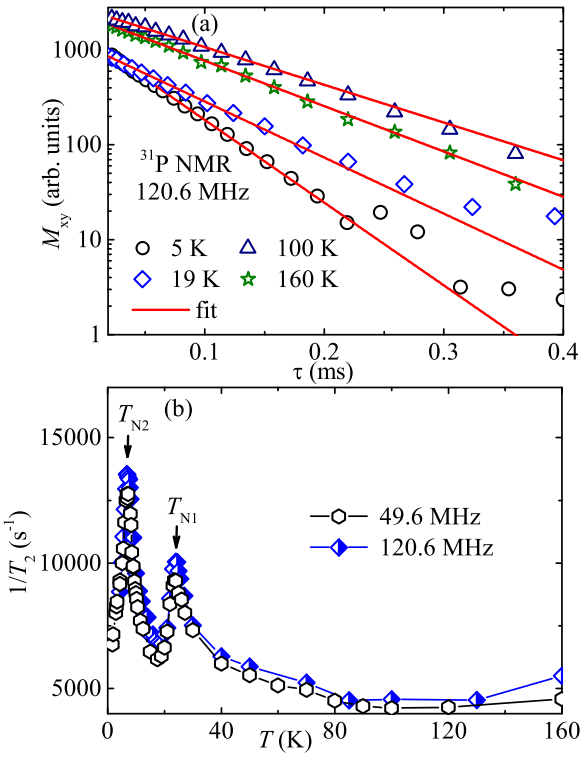


FIG. 10. (a) Transverse magnetization recovery curves as a function of $\tau$ at four different temperatures. The solid lines show the fit using Eq. (7). (b) $^{31}$P NMR spin-spin relaxation rate ($1/T_2$) vs $T$ measured at 49.6 and 120.6 MHz. The downward arrows mark the transition temperatures at $T_{N1} \simeq 23.5$ K and $T_{N2} \simeq 9.5$ K.

alters the magnetic properties significantly. For instance, in the phosphates (CsCl, CsBr, CsI)$Cu_5P_2O_{10}$, the value of $\theta_{CW}$ which represents the overall energy scale of the exchange couplings as well as the value of $T_N$ increase systematically as the halide ion is changed from Cl to I in the order of increasing ionic radius [27]. The obtained values of $\theta_{CW}$ and $T_N$ for RCCPO are comparable to that of the analog compound CCCVO, resulting in an almost identical frustration parameter ($f \simeq 8$ for RCCPO, $f \simeq 7.7$ for CCCVO). A recent theoretical work has shown that upon replacement of $V^{5+}$ by $P^{5+}$ in CCCVO where the ionic radius of $P^{5+}$ is two times smaller than that of $V^{5+}$, the coupling within the kagome layer remains almost the same whereas the coupling between a kagome layer and capped Cu atom becomes five times larger, increasing the degree of frustration within the $OCu_4$ tetrahedra [24]. In this analogy, RCCPO should have a larger $\theta_{CW}$ value than CCCVO because of the replacement of $V^{5+}$ by $P^{5+}$. Here, another difference is that RCCPO contains $Rb^+$ that has a smaller ionic radius than $Cs^+$ in CCCVO, which possibly plays a crucial role due to which the overall energy scale of the exchange couplings is comparable.

In contrast to a single magnetic transition in all phosphate compounds [(CsCl, CsBr, CsI)$Cu_5P_2O_{10}$], there appear two magnetic transitions ($T_{N1} \simeq 20$ K and $T_{N2} \simeq 7$ K) in RCCPO at low temperatures which makes this compound an exception in this series. It is to be noted that, despite having the same crystal structure (monoclinic), their space group symmetry is found to be different ($C2/c$ for RCCPO and $P2_1/c$ for the other phosphates). The $OCu_4$ tetrahedra in RCCPO are highly distorted compared to the other phosphates. In RCCPO, each tetrahedron consists of three inequivalent Cu sites in contrast to two Cu sites in other phosphates. A diligent scrutiny of the crystal structure [see Figs. 1(c)–1(e)] reveals that Cu-Cu bond distances and ∠Cu-O-Cu bond angles in the triangular base of the tetrahedron are inequivalent for RCCPO in contrast to the equilateral triangular base in other phosphates. Similarly, the Cu-Cu bond distances and ∠Cu-O-Cu bond angles of the apical (or capped) Cu with respect to the Cu atoms at the base are all inequivalent for RCCPO in contrast to other phosphates. Moreover, the six Cu-Cu bond distances in the hexagonal ring [Fig. 1(c)] are also found to be unequal and vary from 3.065 to 3.225 Å for RCCPO while this hexagon is isotropic with the same bond distance for all other phosphates. Thus, the strong distortion in the crystal structure could be the reason for having different ground state properties in RCCPO.

Double magnetic transitions are predicted to occur in anisotropic triangular lattice antiferromagnets (TLAFs) when the magnetic anisotropy is of easy-axis type [44,53–55]. On lowering the temperature, the collinear up-up-down state appears before the 120° state and the temperature range of the intermediate phase $(T_{N1} - T_{N2})/T_{N1}$ reflects the relative strength of the easy-axis anisotropy with respect to the isotropic intralayer coupling. Experimentally, double transitions are reported in several TLAFs [56,57,57–59,59]. Double magnetic transitions in zero field are also observed in staircase-kagome magnets $(Mn, Ni, Co)_3V_2O_8$ and $PbCu_3TeO_7$ [14,15,60,61]. In $(Mn, Ni, Co)_3V_2O_8$, both the phases are reported to be incommensurate in nature, originating from two decoupled sublattices in the kagome-staircase structure [62]. However, in RCCPO, the two transitions are different. Our $^{31}$P NMR spectral measurements elucidate probably an incommensurate-type phase below $T_{N1}$ and a commensurate phase below $T_{N2}$. Since the capped-kagome structure is a corner sharing of triangular motifs, the two successive transitions observed can be possibly attributed to anisotropy in the compound. However, a more precise knowledge about the nature and origin of the transitions can only be obtained from neutron scatting experiments and complementary theoretical calculations.

In summary, we present the structural and magnetic properties of a geometrically frustrated quantum magnet $(RbCl)Cu_5P_2O_{10}$. Below $T_t \simeq 310$ K, the monoclinic structure portrays a capped-kagome lattice of $Cu^{2+}$ ions. Sizable magnetic frustration is gauged from a large value of the frustration parameter. The dual magnetic transitions at low temperatures where a commensurate AFM ordering is preceded by an incommensurate ordering in a capped-kagome lattice is unusual and can be possibly ascribed to strong distortion and/or magnetic anisotropy in the spin lattice. Nevertheless, these ambiguous features call for further experimental investigations on this compound.

## ACKNOWLEDGMENTS

We would like to acknowledge SERB, India for financial support bearing sanction Grant No. CRG/2022/000997.

Work at the Ames National Laboratory was supported by the U.S. Department of Energy, Office of Science, Basic Energy Sciences, Materials Sciences and Engineering Division. The Ames National Laboratory is operated for the U.S. Department of Energy by Iowa State University under Contract No. DEAC02-07CH11358.

[1] A. P. Ramirez, Strongly geometrically frustrated magnets, Annu. Rev. Mater. Sci. **24**, 453 (1994).

[2] H. T. Diep, *Frustrated Spin Systems* (World Scientific, Singapore, 2013).

[3] L. Balents, Spin liquids in frustrated magnets, Nature (London) **464**, 199 (2010).

[4] S. Yan, D. A. Huse, and S. R. White, Spin-liquid ground state of the spin-$\frac{1}{2}$ kagome Heisenberg antiferromagnet, Science **332**, 1173 (2011).

[5] T. H. Han, J. S. Helton, S. Chu, D. G. Nocera, J. A. Rodriguez-Rivera, C. Broholm, and Y. S. Lee, Fractionalized excitations in the spin-liquid state of a kagome-lattice antiferromagnet, Nature (London) **492**, 406 (2012).

[6] P. Khuntia, M. Velazquez, Q. Barthélemy, F. Bert, E. Kermarrec, A. Legros, B. Bernu, L. Messio, A. Zorko, and P. Mendels, Gapless ground state in the archetypal quantum kagome antiferromagnet $ZnCu_3(OH)_6Cl_2$, Nat. Phys. **16**, 469 (2020).

[7] M. Fu, T. Ima, T. H. Han, and Y. S. Lee, Evidence for a gapped spin-liquid ground state in a kagome Heisenberg antiferromagnet, Science **350**, 655 (2015).

[8] S. Bieri, L. Messio, B. Bernu, and C. Lhuillier, Gapless chiral spin liquid in a kagome Heisenberg model, Phys. Rev. B **92**, 060407(R) (2015).

[9] T. Picot, M. Ziegler, R. Orús, and D. Poilblanc, Spin-$S$ kagome quantum antiferromagnets in a field with tensor networks, Phys. Rev. B **93**, 060407(R) (2016).

[10] R. Suttner, C. Platt, J. Reuther, and R. Thomale, Renormalization group analysis of competing quantum phases in the $J_1$-$J_2$ Heisenberg model on the kagome lattice, Phys. Rev. B **89**, 020408(R) (2014).

[11] M. Hering, F. Ferrari, A. Razpopov, I. I. Mazin, R. Valenti, H. O. Jeschke, and J. Reuther, Phase diagram of a distorted kagome antiferromagnet and application to Y-kapellasite, npj Comput. Mater. **8**, 10 (2022).

[12] M. Fujihala, K. Morita, R. Mole, S. Mitsuda, T. Tohyama, S. Yano *et al.*, Gapless spin liquid in a square-kagome lattice antiferromagnet, Nat. Commun. **11**, 3429 (2020).

[13] Y. Y. Tang, C. Peng, W. B. Guo, J. F. Wang, G. Su, and Z. Z. He, Octa-kagome lattice compounds showing quantum critical behaviours: Spin gap ground state versus antiferromagnetic ordering, J. Am. Chem. Soc. **139**, 14057 (2017).

[14] E. Morosan, J. Fleitman, T. Klimczuk, and R. J. Cava, Rich magnetic phase diagram of the kagome-staircase compound $Mn_3V_2O_8$, Phys. Rev. B **76**, 144403 (2007).

[15] K. Yoo, B. Koteswararao, J. Kang, A. Shahee *et al.*, Magnetic field-induced ferroelectricity in spin-$\frac{1}{2}$ kagome staircase compound $PbCu_3TeO_7$, npj Quantum Mater. **3**, 45 (2018).

[16] I. Rousochatzakis, A. M. Lauchli, and F. Mila, Highly frustrated magnetic clusters: The kagome on a sphere, Phys. Rev. B **77**, 094420 (2008).

[17] H. O. Jeschke, H. Nakano, and T. Sakai, From kagome strip to kagome lattice: Realizations of frustrated spin-$\frac{1}{2}$ antiferromagnets in Ti(III) fluorides, Phys. Rev. B **99**, 140410(R) (2019).

[18] K. Morita, S. Sota, and T. Tohyama, Resonating dimer-monomer liquid state in a magnetization plateau of a spin-$\frac{1}{2}$ kagome-strip Heisenberg chain, Commun. Phys. **4**, 161 (2021).

[19] Z. L. Dun, J. Trinh, K. Li, M. Lee, K. W. Chen, R. Baumbach, Y. F. Hu *et al.*, Magnetic Ground States of the Rare-Earth Tripod Kagome Lattice $Mg_2RE_3Sb_3O_{14}$ (RE = Gd, Dy, Er), Phys. Rev. Lett. **116**, 157201 (2016).

[20] Z. Dun, X. Bai, J. A. M. Paddison, E. Hollingworth, N. P. Butch, C. D. Cruz, M. B. Stone *et al.*, Quantum Versus Classical Spin Fragmentation in Dipolar Kagome Ice $Ho_3Mg_2Sb_3O_{14}$, Phys. Rev. X **10**, 031069 (2020).

[21] Y. Okamoto, M. Nohara, H. Aruga-Katori, and H. Takagi, Spin-Liquid State in the Spin-$\frac{1}{2}$ Hyperkagome Antiferromagnet $Na_4Ir_3O_8$, Phys. Rev. Lett. **99**, 137207 (2007).

[22] M. J. Lawler, H. Y. Kee, Y. B. Kim, and A. Vishwanath, Topological Spin Liquid on the Hyperkagome Lattice of $Na_4Ir_3O_8$, Phys. Rev. Lett. **100**, 227201 (2008).

[23] A. S. Botana, H. Zheng, S. H. Lapidus, J. F. Mitchell, and M. R. Norman, Averievite: A copper oxide kagome antiferromagnet, Phys. Rev. B **98**, 054421 (2018).

[24] D. Dey and A. S. Botana, Role of chemical pressure on the electronic and magnetic properties of the spin-$\frac{1}{2}$ kagome mineral averievite, Phys. Rev. B **102**, 125106 (2020).

[25] M. Georgopoulou, D. Boldrin, B. Fåk, P. Manuel, A. Gibbs, J. Ollivier, E. Suard, and A. S. Wills, Magnetic ground states and excitations in Zn-doped averieite – a family of oxide-based $S = 1/2$ kagome antiferromagnets, arXiv:2306.14739 [cond-mat.str-el].

[26] T. Biesner, S. Roh, A. Pustogow, H. Zheng, J. F. Mitchell, and M. Dressel, Magnetic terahertz resonances above the Néel temperature in the frustrated kagome antiferromagnet averievite, Phys. Rev. B **105**, L060410 (2022).

[27] M. J. Winiarski, T. T. Tran, J. R. Chamorro, and T. M. McQueen, $(CsX)Cu_5O_2(PO_4)_2$ ($X$ = Cl, Br, I): A family of $Cu^{2+}$ spin-$\frac{1}{2}$ compounds with capped-kagomé networks composed of $OCu_4$ units, Inorg. Chem. **58**, 4328 (2019).

[28] W. Zhang, Z. He, Y. Xie, M. Cui, S. Zhang, S. Chen, Z. Zhao, M. Zhang, and X. Huang, Molybdate–tellurite compounds with capped-kagome spin–lattices, Inorg. Chem. **59**, 2299 (2020).

[29] I. V. Kornyakov, V. A. Vladimirova, O. I. Siidra, and S. V. Krivovichev, Expanding the Averievite Family, $(MX)Cu_5O_2(T^{5+}O_4)_2$ ($T^{5+}$ = P, V; $M$ = K, Rb, Cs, Cu; $X$ = Cl, Br): Synthesis and single-crystal x-ray diffraction study, Molecules **26**, 1833 (2021).

[30] J. R. Carvajal, Recent advances in magnetic structure determination by neutron powder diffraction, Phys. B: Condens. Matter **192**, 55 (1993).

[31] V. P. Bader, J. Langmann, P. Gegenwart, and A. A. Tsirlin, Deformation of the triangular spin-$\frac{1}{2}$ lattice in $Na_2SrCo(PO_4)_2$, Phys. Rev. B **106**, 054415 (2022).

[32] A. A. Tsirlin, R. Nath, A. M. Abakumov, Y. Furukawa, D. C. Johnston, M. Hemmida, H.-A. Krug von Nidda, A. Loidl, C. Geibel, and H. Rosner, Phase separation and frustrated square

lattice magnetism of $Na_{1.5}VOPO_4F_{0.5}$, Phys. Rev. B **84**, 014429 (2011).

[33] S. Guchhait, D. V. Ambika, Q.-P. Ding, M. Uhlarz, Y. Furukawa, A. A. Tsirlin, and R. Nath, Deformed spin-$\frac{1}{2}$ square lattice in antiferromagnetic $NaZnVOPO_4(HPO_4)$, Phys. Rev. B **106**, 024426 (2022).

[34] C. Kittel, *Introduction to Solid State Physics* (Wiley, Hoboken, NJ, 2004).

[35] R. Nath, M. Padmanabhan, S. Baby, A. Thirumurugan, D. Ehlers, M. Hemmida, H.-A. Krug von Nidda, and A. A. Tsirlin, Quasi-two-dimensional $S = \frac{1}{2}$ magnetism of $Cu[C_6H_2(COO)_4][C_2H_5NH_3]_2$, Phys. Rev. B **91**, 054409 (2015).

[36] P. W. Selwood, *Magnetochemistry* (Interscience, New York, 1956); G. A. Bain and J. F. Berry, Diamagnetic corrections and Pascal's constants, J. Chem. Educ. **85**, 532 (2008)..

[37] S. Guchhait, Q. P. Ding, M. Sahoo, A. Giri, S. Maji, Y. Furukawa, and R. Nath, Quasi-one-dimensional uniform spin-$\frac{1}{2}$ Heisenberg antiferromagnet $KNaCuP_2O_7$ probed by $^{31}P$ and $^{23}Na$ NMR, Phys. Rev. B **103**, 224415 (2021).

[38] S. S. Islam, K. M. Ranjith, M. Baenitz, Y. Skourski, A. A. Tsirlin, and R. Nath, Frustration of square cupola in $Sr(TiO)Cu_4(PO_4)_4$, Phys. Rev. B **97**, 174432 (2018).

[39] S. S. Islam, V. Singh, K. Somesh, P. K. Mukharjee, A. Jain, S. M. Yusuf, and R. Nath, Unconventional superparamagnetic behavior in the modified cubic spinel compound $LiNi_{0.5}Mn_{1.5}O_4$, Phys. Rev. B **102**, 134433 (2020).

[40] P. K. Mukharjee, K. M. Ranjith, B. Koo, J. Sichelschmidt, M. Baenitz, Y. Skourski, Y. Inagaki, Y. Furukawa, A. A. Tsirlin, and R. Nath, Bose-Einstein condensation of triplons close to the quantum critical point in the quasi-one-dimensional spin-$\frac{1}{2}$ antiferromagnet $NaVOPO_4$, Phys. Rev. B **100**, 144433 (2019).

[41] A. Yogi, N. Ahmed, R. Nath, A. A. Tsirlin, S. Kundu, A. V. Mahajan, J. Sichelschmidt, B. Roy, and Y. Furukawa, Antiferromagnetism of $Zn_2VO(PO_4)_2$ and the dilution with $Ti^{4+}$, Phys. Rev. B **91**, 024413 (2015).

[42] M. Kontani, T. Hioki, and Y. Masuda, Hyperfine fields in an incommensurate antiferromagnetic Cr-Mo alloy system, J. Phys. Soc. Jpn. **39**, 672 (1975).

[43] H. Sakurai, N. Tsuboi, M. Kato, K. Yoshimura, K. Kosuge, A. Mitsuda, H. Mitamura, and T. Goto, Antiferromagnetic order in the two-dimensional spin system $Cu_3B_2O_6$, Phys. Rev. B **66**, 024428 (2002).

[44] K. M. Ranjith, R. Nath, M. Majumder, D. Kasinathan, M. Skoulatos, L. Keller, Y. Skourski, M. Baenitz, and A. A. Tsirlin, Commensurate and incommensurate magnetic order in spin-1 chains stacked on the triangular lattice in $Li_2NiW_2O_8$, Phys. Rev. B **94**, 014415 (2016).

[45] K. M. Ranjith, M. Majumder, M. Baenitz, A. A. Tsirlin, and R. Nath, Frustrated three-dimensional antiferromagnet $Li_2CuW_2O_8$: $^7Li$ NMR and the effect of nonmagnetic dilution, Phys. Rev. B **92**, 024422 (2015).

[46] Y. Yamada and A. Sakata, An analysis method of antiferromagnetic powder patterns in spin-echo NMR under external fields, J. Phys. Soc. Jpn. **55**, 1751 (1986).

[47] J. Kikuchi, K. Ishiguchi, K. Motoya, M. Itoh, K. Inari, N. Eguchi, and J. Akimitsu, Nmr and neutron scattering studies of quasi one-dimensional magnet $CuV_2O_6$, J. Phys. Soc. Jpn. **69**, 2660 (2000).

[48] D. C. Johnston, S.-H. Baek, X. Zong, F. Borsa, J. Schmalian, and S. Kondo, Dynamics of Magnetic Defects in Heavy Fermion $LiV_2O_4$ from Stretched Exponential $^7Li$ NMR Relaxation, Phys. Rev. Lett. **95**, 176408 (2005).

[49] T. Moriya, Nuclear magnetic relaxation in antiferromagnetics, Prog. Theor. Phys. **16**, 23 (1956).

[50] D. Beeman and P. Pincus, Nuclear spin-lattice relaxation in magnetic insulators, Phys. Rev. **166**, 359 (1968).

[51] M. Belesi, F. Borsa, and A. K. Powell, Evidence for spin-wave excitations in the long-range magnetically ordered state of a $Fe_{19}$ molecular crystal from proton NMR, Phys. Rev. B **74**, 184408 (2006).

[52] R. Nath, Y. Furukawa, F. Borsa, E. E. Kaul, M. Baenitz, C. Geibel, and D. C. Johnston, Single-crystal $^{31}P$ NMR studies of the frustrated square-lattice compound $Pb_2(VO)(PO_4)_2$, Phys. Rev. B **80**, 214430 (2009).

[53] F. Matsubara, Magnetic ordering in a hexagonal antiferromagnet, J. Phys. Soc. Jpn. **51**, 2424 (1982).

[54] S. Miyashita and H. Kawamura, Phase transitions of anisotropic Heisenberg antiferromagnets on the triangular lattice, J. Phys. Soc. Jpn. **54**, 3385 (1985).

[55] G. Quirion, M. Lapointe-Major, M. Poirier, J. A. Quilliam, Z. L. Dun, and H. D. Zhou, Magnetic phase diagram of $Ba_3CoSb_2O_9$ as determined by ultrasound velocity measurements, Phys. Rev. B **92**, 014414 (2015).

[56] M. Lee, J. Hwang, E. S. Choi, J. Ma, C. R. Dela Cruz, M. Zhu, X. Ke, Z. L. Dun, and H. D. Zhou, Series of phase transitions and multiferroicity in the quasi-two-dimensional spin-$\frac{1}{2}$ triangular-lattice antiferromagnet $Ba_3CoNb_2O_9$, Phys. Rev. B **89**, 104420 (2014).

[57] H. D. Zhou, C. Xu, A. M. Hallas, H. J. Silverstein, C. R. Wiebe, I. Umegaki, J. Q. Yan, T. P. Murphy, J.-H. Park, Y. Qiu, J. R. D. Copley, J. S. Gardner, and Y. Takano, Successive Phase Transitions and Extended Spin-Excitation Continuum in the spin-$\frac{1}{2}$ Triangular-Lattice Antiferromagnet $Ba_3CoSb_2O_9$, Phys. Rev. Lett. **109**, 267206 (2012).

[58] K. M. Ranjith, K. Brinda, U. Arjun, N. G. Hegde, and R. Nath, Double phase transition in the triangular antiferromagnet $Ba_3CoTa_2O_9$, J. Phys.: Condens. Matter **29**, 115804 (2017).

[59] K. Yokota, N. Kurita, and H. Tanaka, Magnetic phase diagram of the spin-$\frac{1}{2}$ triangular-lattice Heisenberg antiferromagnet $Ba_3CoNb_2O_9$, Phys. Rev. B **90**, 014403 (2014).

[60] R. C. Rai, J. Cao, S. Brown, J. L. Musfeldt, D. Kasinathan, D. J. Singh, G. Lawes, N. Rogado, R. J. Cava, and X. Wei, Optical properties and magnetic-field-induced phase transitions in the ferroelectric state of $Ni_3V_2O_8$: Experiments and first-principles calculations, Phys. Rev. B **74**, 235101 (2006).

[61] N. R. Wilson, O. A. Petrenko, and L. C. Chapon, Magnetic phases in the Kagomé staircase compound $Co_3V_2O_8$ studied using powder neutron diffraction, Phys. Rev. B **75**, 094432 (2007).

[62] C. Dong, J. F. Wang, Z. Z. He, Y. T. Chang, M. Y. Shi, Y. R. Song, S. M. Jin, Y. Q. Du, Z. Y. Wu, X. T. Han, K. Kindo, and M. Yang, Reentrant ferroelectric phase induced by a tilting high magnetic field in $Ni_3V_2O_8$, Phys. Rev. B **105**, 024427 (2022).